PCCP

Accepted Manuscript

ROYAL SOCIETY OF CHEMISTRY

www.rsc.org/pccp

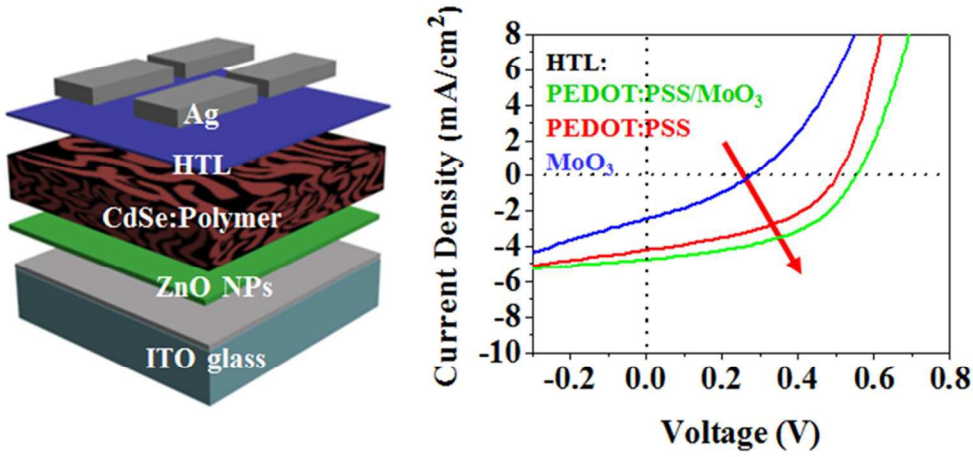

80x39mm (300 x 300 DPI)

Journal Name

ARTICLE

Inverted hybrid CdSe-polymer solar cells adopting PEDOT:PSS/MoO_3 as dual hole transport layers†

Received 00th January 20xx,
Accepted 00th January 20xx

DOI: 10.1039/x0xx00000x

www.rsc.org/

Leize Zhu, Beau J. Richardson, and Qiuming Yu*

Inverted CdSe quantum dots (QDs):poly (3-hexylthiophene) (P3HT) organic/inorganic hybrid solar cells (OIHSCs) with the PEDOT:PSS/MoO_3 dual hole transport layers (HTLs) showed superior performance over those with a single HTL of PEDOT:PSS or MoO_3. The enhanced electron blocking at the active layer/anode interface as well as the prevention of leakage current accounted for the enhancement in the efficiency of the solar cells with the dual HTLs. By adopting the inverted structure and using the dual HTLs, the resistive losses of the CdSe QDs:P3HT hybrid system at high illumination power were effectively prevented. Further study showed the structure of dual HTLs was applicable to the solar cells with CdSe QDs and nanorods (NRs) blended with poly(thienothiophene-co-benzodithiophenes)7-F20 (PTB7-F20).

Introduction

Organic/inorganic hybrid solar cells (OIHSCs) are attractive for the photovoltaic (PV) research community as an alternative to all-organic solar cells. OIHSCs combine the advantages of the tunable band gap[1] and facilitated charge transport[2] enabled by inorganic semiconductor quantum dots (QDs) or nanorods (NRs) and the flexibility, light weight, and low-cost fabrication offered by conjugated semiconducting polymers[3]. They typically adopt a bulk heterojunction (BHJ) structure with the inter-mixing of polymers as an acceptor and inorganic semiconductors as a donor in a single active layer. Polymers such as poly (3-hexylthiophene) (P3HT)[2, 4], poly[2, 6-(4, 4-bis(2-ethylhexyl)-4H-cyclopenta[2, 1-b:3, 4-b0]-dithiophene)-alt-4, 7-(2, 1, 3-benzothiadiazole)] (PCPDTBT)[5, 6], poly[2-methoxy-5-(2-ethylhexyloxy)-1, 4-phenylenevinylene] (MEH-PPV)[7, 8], and poly({4, 8-bis[(2-ethylhexyl)oxy]benzo[1, 2-b:4, 5-b′]dithiophene-2, 6-diyl}{3-fluoro-2-[(2-ethylhexyl)carbonyl]thieno[3, 4-b]thiophenediyl}) (PTB7)[9] and their derivatives are commonly used as the donor. The acceptors are the inorganic semiconductors such as CdSe[2], CdS[10, 11], and PbS[12] QDs or NRs. These inorganic semiconductors offer enhanced absorption in the solar spectrum region and generate extra excitons in addition to the polymer part. The nanoscale phase separation creates a high density of donor/acceptor interfaces to enable exciton dissociation and the subsequent charge transportation in the donor and acceptor domains[13].

OIHSCs are typically fabricated with a conventional device configuration of ITO/hole transport layer (HTL)/BHJ/Al, where ITO acts as the bottom hole-collecting anode and a low work function metal (e.g., Al) as the top electron-collecting cathode. Poly(3, 4-ethylenedioxythiophene)-poly(styrenesulfonate) (PEDOT:PSS) is used as an HTL due to its broad applicability, ease of use, and availability[4]. The active layer is a mixture of inorganic semiconductor QDs or NRs and polymers. Until now, the highest power conversion efficiency (PCE) of 3.64 % was achieved by using a blend of CdSe QDs and NRs as the donor and P3HT as the acceptor with a conventional configuration[5]. However, OIHSCs with a conventional configuration are unstable because indium is able to diffuse into the polymer layer and thus degrade the performance of OIHSCs[14]. In addition, prolonged exposure of conventional configuration devices to air and moisture can cause oxidation of the top electrode as well as degradation of the active layer[15]. Finally, direct deposition of metal onto the active layer may lead to either metal diffusion into the film or metal reaction with the polymer, and thus adversely affect the semiconducting properties of the polymer[16, 17].

Regarding these issues raised by adopting a conventional structure, an inverted device configuration was developed with a typical structure of ITO/electron transport layer (ETL)/BHJ/HTL/Ag. In these devices, an air-stable high work function metal (e.g., Ag or Au) is placed on top as the anode while the bottom ITO is used as the cathode. An ETL (e.g., ZnO) is inserted between the ITO and the active layer to selectively extract electrons to the cathode. The presence of an ETL greatly reduces the leakage current in the devices and prevents the diffusion of indium into the active layer. An HTL is inserted between the active layer and the anode to selectively extract holes while concurrently blocking electrons, thereby further reducing the dark (leakage) current and increasing the open-circuit voltage (V_{OC}) and fill factor (FF). The high work function of PEDOT:PSS (4.8-5.2 eV) is typically used as the HTL[18]. PEDOT:PSS helps the anode to form ohmic contact with

Department of Chemical Engineering, University of Washington, Seattle, WA 98195, USA E-mail: qyu@uw.edu

† Electronic Supplementary Information (ESI) available: See DOI: 10.1039/x0xx00000x

the BHJ active layer to improve the V_{OC} and charge-collecting ability of solar cells[19]. However, PEDOT:PSS suffers from several drawbacks including large electrical and microstructural inhomogeneities[20], poor electron blocking property[21], and the tendency of eroding the electrodes[22]. Various transition metal oxides such as nickel oxide (NiO)[23, 24], molybdenum oxide (MoO_3)[19, 25], vanadium oxide (V_2O_5)[26], and tungsten oxide (WO_3)[27] were developed to use as an alternative HTL to PEDOT:PSS. Among these, MoO_3 is one of the most promising materials because of its nontoxic nature, very deep-lying electronic states, and strongly n-doped character caused by oxygen vacancies[28]. Inverted devices fabricated using MoO_3 as the HTL consistently show higher PCE than conventional devices using PEDOT:PSS as the bottom electrode interlayer[29, 30]. Despite the fact that the inverted configuration has been extensively used in fabricating all-organic solar cells, only a few works have been reported regarding OIHSCs with an inverted structure. An inverted binary OIHSC was fabricated by using CdSe NRs as the acceptor and P3HT as the donor. CdSe NR arrays were deposited on TiO_2-coated ITO glass[31]. The interstitial spaces between the nanorods were infiltrated with P3HT and the devices were completed with a Au top electrode. The best power conversion efficiency was achieved at 1.38% under 100 mW cm^{-2} of AM 1.5G illumination. Inverted ternary OIHSCs were developed to improve the binary polymer solar cells. Inverted hybrid solar cells based on pyrite FeS_2 nanocrystals in P3HT:PCBM were fabricated with a structure of ITO/ZnO/P3HT:PCBM:FeS_2/PEDOT:PSS/Ag. The devices showed enhanced photocurrent and great air-stability after aging 28 days exposed in air. Additionally, solar cells with a structure of ITO/TiO_2/PCDTBT:PCBM:CdSe QDs/MoO_3/Ag were constructed. By the incorporation of CdSe QDs into binary PCDTBT:PCBM polymer solar cells, the inverted devices showed enhancement of the V_{OC}, short-circuit current density (J_{SC}), and FF, and thus an improved PCE of 6.94%[32]. Very recently, a MoO_3:PEDOT:PSS hybrid ink was developed by mixing MoO_3 nanoparticles with PEDOT:PSS and deployed as the HTL in the inverted organic solar cells with P3HT:PCBM and PTB7:PCBM active layers. The inverted organic solar cells with the hybrid HTL achieved comparable PCEs as those using the thermally evaporated MoO_3 HTL when the thickness of MoO_3 is greater than 20 nm. The solution processability along with the less thickness dependence of device performance makes this HTL hybrid ink more compatible with roll-to-roll printing process[33].

In this work, we fabricated inverted hybrid CdSe-polymer solar cells with a structure of ITO/ZnO/CdSe:polymer/HTL/Ag. Two widely used conjugated semiconducting polymers P3HT and PTB7 were blended with CdSe QDs or QDs + NRs to form the hybrid BHJ layers. First, three types of HTLs including two single HTLs, PEDOT:PSS and MoO_3, and a dual HTL, PEDOT:PSS/MoO_3, were inserted between the active layer of CdSe QDs:P3HT and the top anode. Different from the previous work using the mixture of MoO_3:PEDOT:PSS as a hybrid ink for HTL[33], we spin-coated a layer of PEDOT:PSS first and then thermally evaporated a layer of MoO_3, which serves as a dual HTL. The performance of the fabricated inverted hybrid solar cells was evaluated. Hole mobility and electron mobility were obtained by applying the space-charge-limited-current (SCLC) method to the hole-only and electron-only devices with the same hybrid active layer, respectively. External quantum efficiency (EQE) measurements were performed in order to understand the photon absorption and charge carrier generation processes. An improved Shockley model using the space-charge approach was applied to fit the dark J-V curves to obtain the shunt resistance (R_{SH}) and series resistance (R_S), which were used to understand the different performance observed in the devices using the three types of HTLs. The enhancement in efficiency of the fabricated solar cells was ascribed to improved electron blocking at the active layer/anode interface as well as to prevention of leakage current. By adopting the inverted structure and using the dual HTLs, the resistive losses of CdSe:P3HT hybrid system at high illumination power are effectively prevented. Further study showed that dual HTLs were applicable to CdSe:PTB7-F20 solar cells. An efficiency as high as 2.35% was reached by inverted hybrid CdSe-PTB7-F20 solar cells with a structure of ITO/ZnO/CdSe QDs + NRs:PTB7-F20/HTL/Ag.

Experimental

Chemicals

Cadmium oxide (CdO, ≥99.99%), selenium powder (Se, 99.99%), trioctylphosphine oxide (TOPO, 99%), oleic acid (≥ 99.0%), and zinc oxide nanoparticle (ZnO NP) dispersion (50 wt% in H_2O and the particle size < 100 nm determined using dynamic light scattering (DLS)) were purchased from Sigma-Aldrich. Trioctylphosphine (TOP, 97%) and n-tetradecylphosphonic acid (TDPA, 97%) were obtained from Strem Chemicals Inc. P3HT (4002-E) was purchased from Rieke Metals, Inc. Poly(thienothiophene-co-benzodithiophenes)7-F20 (PTB7-F20) was obtained from 1-Material, Inc. PEDOT:PSS (Clevios P VP AI4083) was obtained from H.C. Starck and filtered through a 0.22 μm nylon filter before use. MoO_3 powder (99.9995%) was purchased from Alfa Aesar. Ag pellets (99.99%) and ITO coated glass were obtained from R.D. Mathis and Colorado Concept Coatings LLC, respectively.

CdSe QD synthesis and ligand exchange

CdSe QDs were synthesized by the hot injection method[11]. Briefly, CdO (0.5 mmol), oleic acid (10.0 mmol), and TOPO (2.5 mmol) were mixed and heated to 280°C under N_2 protection. In a separate airtight tube, 0.5 mmol of Se was dissolved in 1.5 ml of TOP to form a TOP-Se solution at 150°C. Subsequently, 1.5 ml of TOP-Se solution was swiftly injected into the three-neck flask using a glass syringe. After the injection, the temperature was maintained at 280°C for 2 to 30 min in order to obtain CdSe QDs with the size from 4.0 to 7.4 nm. The reaction was quenched by adding 5 ml toluene. CdSe QDs were purified by washing with toluene and being precipitated in methanol for three cycles. QDs were ligand exchanged with pyridine overnight at 60°C. The ligand exchanged QDs were then precipitated by adding hexane, separated by

centrifugation at 6000 rpm for 2 min, and re-dispersed in 1.0 ml pyridine:chlorobenzene (1:20 vol/vol).

CdSe NRs synthesis and ligand exchange

CdSe NRs were synthesized according to the reported protocol[34] with a few modifications. Typically, CdO (0.4 mmol), TDPA (1.1 mmol), and TOPO (10.6 mmol) were mixed and heated to 300°C under N_2 protection to dissolve CdO in the TDPA/TOPO solution. After an optically clear solution was obtained, it was heated up to 320°C. In a separate airtight tube, 0.5 mmol of Se was dissolved in 4.0 ml of TOP to form the injection solution at 150°C. This solution was injected into the reaction flask at 320°C by using a 5-ml glass syringe. After the injection, the temperature of the reaction mixture dropped down and was kept at 250°C for the growth. The reaction was stopped at 30 min by removing the heating mantle. The purification and ligand exchange procedures of CdSe NRs were the same as those of CdSe QDs.

Device fabrication

Inverted OIHSCs were fabricated on ITO coated glass substrates with a sheet resistance = 10 Ω sq^{-1}. The substrates used for all devices were first cleaned by several ultrasonication steps in soapy deionized (DI) water, DI water, acetone, and isopropanol, each for 15 min. The cleaned substrates were treated with oxygen plasma for 30 s prior to depositing any films. The substrates were first spin-coated with a 5.22 wt% ZnO NP dispersion at 3000 rpm for 30 s. After being baked in air at 120°C for 10 min, the substrates were transferred to a nitrogen glovebox for the spin coating of CdSe-polymer layers. The CdSe-polymer solutions were prepared by dissolving CdSe QDs or NRs and P3HT or PTB7-F20 in pyridine:chlorobenzene (1:20 vol/vol) to a total concentration of 30 mg ml^{-1}. The weight ratio of CdSe QDs in the mixture was 80 or 85 wt%. The weight ratio of QDs to NRs was 2:1 for the devices containing the mixture of CdSe QDs + NRs:PTB7-F20. The CdSe-polymer layers were fabricated by spin-coating of CdSe-polymer solutions at 1000 rpm for 30 s, followed by being baked at 150°C for 10 min. Three types of HTLs were inserted between the active layer and the top Ag anode. The 40 nm PEDOT:PSS layer was fabricated by spin-coating a dilute PEDOT:PSS solution at 5000 rpm and baking at 120°C for 10 min. The 10 nm MoO_3 layer was fabricated by thermal evaporation. The dual HTLs of 40 nm PEDOT:PSS/10 nm MoO_3 were fabricated by spin-coating a dilute PEDOT:PSS solution and followed by thermal deposition of the MoO_3 layer. Finally, a 100 nm Ag layer was thermally evaporated through a shadow mask to make four electrodes each with an area of 10 mm^2. The background pressure was kept below 10^{-6} Torr during the deposition.

The electron-only devices were fabricated with a structure of 100 nm Al/85 wt% CdSe QDs:P3HT/100 nm Al. A 100 nm thick Al layer was thermally evaporated onto a glass substrate and then the CdSe QDs:P3HT solution was spin-coated on the Al-covered substrate followed by the deposition of a 100 nm thick Al layer. The area for those electron-only devices was 10 mm^2. Similarly, the hole-only devices were fabricated for the measurement of hole mobility in the hybrid thin film with a structure of ITO/40 nm PEDOT:PSS/85 wt% CdSe QDs:P3HT/100 nm Au. A layer of 40 nm PEDOT:PSS was spin-coated on an ITO coated glass substrate and baked at 105°C for 20 min, followed by spin-coating of the active layer. Finally, a 100 nm Au was deposited onto the active layer.

Characterization

UV-Vis spectra of CdSe QDs and NRs in toluene were acquired using a Varian Cary 5000 UV-Vis-NIR spectrophotometer from the wavelength of 450 to 750 nm. Photoluminescence (PL) spectra of the same solutions were recorded by Perkin Elmer LS-50B Fluorimeter with an excitation wavelength of 450 nm. Transmission electron microscopy (TEM) images were acquired using an FEI Tecnai G2 F20 TEM operating at an accelerating voltage of 200 kV. The samples for TEM analysis were prepared by drop casting a dilute solution of NCs in chloroform onto ultrathin carbon-coated copper grids. The film thickness was measured using an Alpha-Step 500 profilometer (KLA-Tencor, San Jose, CA). The illuminated current density-voltage (J-V) curves were recorded in a glove box under nitrogen atmosphere using a Keithley 2400 source meter unit. The measurements were performed under AM1.5 illumination condition at an intensity of 100 mW/cm^2. The light intensity was calibrated to 100 mW/cm^2 using a calibrated silicon solar cell that had been previously standardized at the National Renewable Energy Laboratory. The J-V curves of the hole-only and the electron-only devices were measured using the same set-up under dark. External quantum efficiency (EQE) spectra were gathered in air using an Oriel Xenon lamp (450 W) with an AM 1.5 filter, a monochromator (Oriel Cornerstone 130 1/8 m), a chopper with a frequency of 100 Hz, a lock-in amplifier (SR830, Stanford Research Corp), and a Si-based diode (J115711-1-Si detector) for calibration.

Results and discussion

Inorganic semiconductor QDs or NRs in OIHSCs absorb sunlight to generate electron-hole pairs. The connected inorganic semiconductor phase serves as a pathway to transport electrons. The size of CdSe QDs not only affects the light absorption but also the efficiency of electron transfer and the mixing uniformity with polymers. It was reported that CdSe QDs with the size of 6.5±0.5 nm blended with P3HT generated a PCE of 1.7±0.1% for the devices with a conventional configuration[35]. Larger size CdSe QDs of 8-10 nm induced the aggregation of QDs in the mixtures, which causes a poor electrical contact between the active layer and the electrodes and poor reproducibility of device performance[36]. CdSe QDs with the size below 6 nm resulted in large hopping distances among QDs in the active layer, leading to insufficient percolation pathway for the electron transport. As a result, a small J_{SC} was commonly observed in those devices[37].

Table 1 Summary of the performance parameters of inverted hybrid CdSe QDs:P3HT solar cells under AM 1.5G 1-sun illumination. Devices were fabricated with a structure of ITO/ZnO/85 wt% CdSe QDs:P3HT/HTL/Ag. A MoO_3 only, a PEDOT:PSS only, or a PEDOT:PSS/MoO_3 were used as the HTL. The thickness of PEDOT:PSS and MoO_3 are 40 and 10 nm, respectively.

HTLs	V_{OC} (V)	J_{SC} (mA/cm^2)	FF (%)	PCE (%)	PCE_{max} (%)	R_s (Ω)	R_{sh} (Ω)
PEDOT:PSS/ MoO_3	0.55±0.02	4.96±0.13	47.6±2.4	1.37±0.23	1.53	3.45	29705.6
PEDOT:PSS	0.50±0.01	4.22±0.23	43.2±2.5	0.85±0.06	0.88	2.05	27005.4
MoO_3	0.28±0.05	2.45±0.32	31.9±3.3	0.22±0.23	0.41	3.07	2396.9

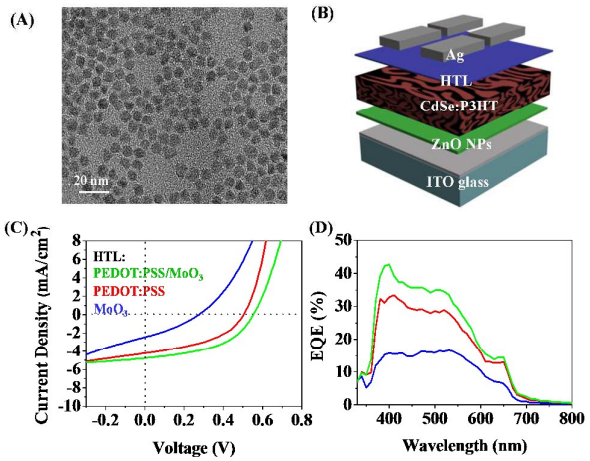

Fig. 1 (A) A TEM image of CdSe QDs synthesized with the average size of 6.3 ± 0.2 nm. (B) Schematic of an inverted OIHSC with CdSe QDs:P3HT as the active layer. (C) Typical J-V characteristics of the inverted devices under 1 sun AM 1.5G solar illumination. (D) EQE as a function of the wavelength of those inverted solar cells. Devices were fabricated with a structure of ITO/ZnO/85 wt% CdSe QDs:P3HT/HTL/Ag. A MoO_3 only, a PEDOT:PSS only, or a PEDOT:PSS/MoO_3 were used as the HTL. The thickness of PEDOT:PSS and MoO_3 are 40 and 10 nm, respectively.

Therefore, CdSe QDs with a size around 6-7 nm were synthesized. The reaction time was controlled from 2 to 30 min at 280°C and the UV-Vis and PL spectra of the synthesized CdSe QDs were measured. The first excitonic absorption peak shifts from 604 to 654 nm as shown in the UV-Vis spectra in Fig. S1A. The corresponding PL emission changes from 619 to 660 nm with the excitation wavelength of 450 nm (Fig. S1B). The diameter of the synthesized CdSe QDs was estimated by using the empirical fitting function that correlates the diameter of CdSe QDs to the wavelength of the first excitonic absorption peak[38] and the values of 4.0, 4.3, 5.0, 6.1, and 7.4 nm were obtained. The morphology and size of the synthesized CdSe QDs were also studied using TEM. Fig. 1A shows a TEM image of CdSe QDs synthesized by reacting at 280°C for 5 min. The QDs are spherical particles and the average diameter is 6.3±0.2 nm calculated by counting 200 particles, which is in good agreement with the value of 6.1 nm determined from the empirical fitting equation[38]. These CdSe QDs were used to fabricate all the devices reported in this work.

Inverted hybrid CdSe-polymer solar cells were first made with the active layer of CdSe QDs:P3HT and the architecture is shown in Fig. 1B. A ZnO NP layer with a thickness of 36±3 nm was used as the ETL. An HTL was inserted between the Ag anode and the active layer. Three types of HTL: 40 nm PEDOT:PSS, 10 nm MoO_3, and 40 nm PEDOT:PSS/10 nm MoO_3, were investigated. The device performance is summarized in Table 1. Fig. 1C shows the typical J-V characteristics of the fabricated devices under 1 sun (= 100 mW/cm^2) AM1.5 G simulated solar illumination. For the devices containing 85 wt% CdSe QDs with the single HTL of MoO_3, a J_{SC} of 2.45±0.32 mA/cm^2, a V_{OC} of 0.28±0.05 V and a FF of 31.9±3.3% were obtained, which leads to an overall PCE of 0.22±0.23%. Using PEDOT:PSS as the single HTL greatly improved the J_{SC}, V_{OC}, and FF of the devices to the values of 4.22±0.23 mA/cm^2, 0.50±0.01 V, and 43.2±2.5%, respectively, leading to an overall PCE of 0.85±0.06%. The device performance was further improved by the deposition of 10 nm MoO_3 on top of the spin-coated PEDOT:PSS. A PCE as high as 1.37±0.23% was achieved because of the further increase in J_{SC}, V_{OC}, and FF. This PCE of the inverted hybrid BHJ solar cells with the dual HTLs is comparable to the PCE of the conventional hybrid solar cells containing the active layer of P3HT and CdSe QDs, where the QDs were also ligand exchanged with pyridine[37, 39]. The devices with the active layers containing 80 wt% of CdSe QDs exhibited a worse performance than those with 85 wt% of CdSe QDs and the same HTL as shown in Table S1 and Fig. S2. The inferior performance of the devices with a lower weight ratio of CdSe QDs in the active layer is ascribed to the increased hopping distances between the QDs in the active layer, thereby forming insufficient percolation pathways for electron transport[40, 41]. The effect of different HTLs on the performance of devices with 80 wt% CdSe QDs follows the same trend as those with 85 wt% CdSe QDs. The PCEs of these devices are 0.18±0.19%, 0.74±0.01%, and 0.94±0.18% with MoO_3, PEDOT:PSS, and PEDOT:PSS/MoO_3 as the HTL, respectively.

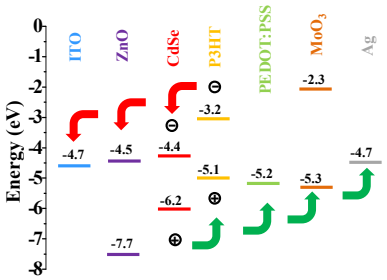

Fig. 2 The energy band diagrams of the materials used in the inverted hybrid CdSe QDs:P3HT solar cells. The energies (in eV) are all referenced from the vacuum level.

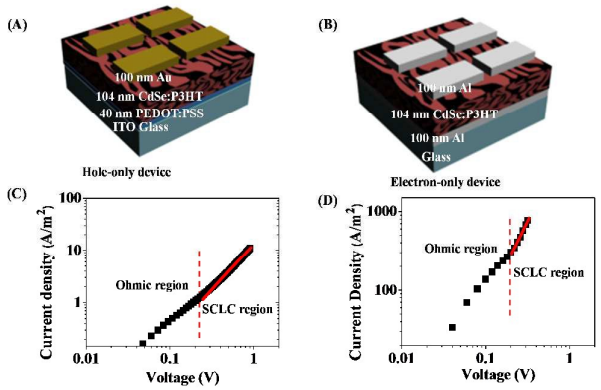

Fig. 3 (A) and (B) Schematics of a hole-only and an electron-only device, respectively. (C) and (D) The dark J-V characteristics of a hole-only and an electron-only device, respectively. The solid lines are fit to the SCLC regions using Eq. 1. The active layers in hole-only and electron-only devices are composed of 85 wt% of CdSe QDs and P3HT.

EQE measurements of devices with 85 wt% CdSe QDs in the BHJ layer and PEDOT:PSS, MoO_3, or PEDOT:PSS/MoO_3 as the HTL were performed in order to understand the photon absorption and charge carrier generation processes. As can be seen from Fig. 1D, the EQE curves correlate well with the absorption of P3HT since most of the photo-generated charge carriers are created in P3HT. By comparing the absorption spectrum of 6.1 nm CdSe QDs (Fig. S1A) with the EQE spectrum (Fig. 1D), one can clearly see that the shoulder around 650 nm is due to the photon-generated charge carriers from CdSe QDs. By integrating the area underneath the EQE curves from the wavelength of 330 to 800 nm, the J_{SC}'s were determined to be 2.41, 4.15, and 4.83 mA/cm^2 for the devices with MoO_3, PEDOT:PSS, or PEDOT:PSS/MoO_3 as the HTL. The calculated J_{SC}'s concord very well with those determined from the J-V measurements (Table 1).

In order to understand the effect of different HTLs on the device performance, we first compared the energy levels of the materials used to fabricate the devices. The energy band diagram of the materials involved in the inverted hybrid devices is displayed in Fig. 2. The band gap of the 6.1 nm CdSe QDs is estimated to be 1.8 eV from the first absorption onset of the UV-Vis spectrum[42]. The conduction and valence band edges (E_{CB} and E_{VB}) are derived to be -4.4 and -6.2 eV, respectively, by considering the quantum confinement effect[43]. The E_{CB} of MoO_3 (-2.3 eV) is higher than that of the 6.1 nm CdSe QDs (-4.4 eV) and the lowest unoccupied molecular orbital (LUMO) of P3HT (-3.2 eV). Thus, the introduction of a MoO_3 layer prevents the transfer of electrons from the active layer to the anode. Meanwhile, the lower E_{VB} of MoO_3 (−5.3 eV) compared to the highest occupied molecular orbital (HOMO) of P3HT (−5.1 eV) creates a small barrier for hole extraction. For PEDOT:PSS, a slightly higher work function of −5.2 eV could be beneficial for the hole extraction but it does not have the ability to block electrons.

Surface roughness of the active layer and the coverage of the HTL could also play roles. We noticed that the surfaces of the hybrid active layers are quite rough from the atomic force microscopy (AFM) topographic images (Fig. S3). It is likely that the surface of the active layer cannot be fully covered by the deposition of a 10 nm MoO_3 layer, which could create direct contact points between the active layer and the anode. In contrast, the spin-coated 40 nm PEDOT:PSS layer alleviates these defects and reduces the shorts between the active layer and the anode. Therefore, devices with the dual HTLs containing PEDOT:PSS and MoO_3 show the best device performance.

The transport properties of electrons and holes in the active layer significantly affect the performance of the fabricated solar cells. In an efficient solar cell, high electron and hole mobility is preferred because this means charge carriers can be transported to the respective electrodes quickly, which suppresses current losses via recombination. The hole-only and electron-only devices were constructed in order to obtain the electron and hole mobility in the active layer. The structures of ITO/PEDOT:PSS/85 wt% CdSe QDs:P3HT/Au (Fig. 3A) and Al/85 wt% CdSe QDs:P3HT/Al (Fig. 3B) were adopted for the hole-only and electron-only devices, respectively. The work functions of Au and Al are -5.2 and -4.3 eV, respectively. The mobility can be obtained by fitting the part of the dark J-V curve under high forward bias, the so-called space-charge-limited-current (SCLC) regime, where the built-in voltage created by space-charge becomes significant at high electric fields. The J-V curves of the hole-only and electron-only devices were measured in the dark (Fig. 3C and 3D). The SCLC regimes were fitted to Mott-Gurney's Law including the Frenkel effect (Eq. 1)[44]

$$J = \frac{9}{8}\mu\varepsilon\varepsilon_0\frac{V^2}{L^3}\exp\left(\frac{0.89\beta}{\sqrt{L}}\sqrt{V}\right) \quad (1)$$

where J is the current density, V the applied voltage, L the active layer thickness, μ the mobility, ε the relative permittivity, ε_0 the permittivity of free space, and β the field-activation factor. The fitted lines are displayed in Fig. 3C and 3D and the fitting parameters are listed in Table S2. Hole mobility was determined to be 1.8 × 10^{-6} cm^2(V•s)$^{-1}$, which concords very well with the reported value of 2.6 × 10^{-6} cm^2(V•s)$^{-1}$ [45]. Electron mobility was determined to be 1.1 × 10^{-3} cm^2(V•s)$^{-1}$, which is higher than the literature values that are in the range of 10^{-4} to 10^{-6} cm^2(V•s)$^{-1}$ [36, 46]. A higher electron

mobility indicates shorter interparticle separation[47] and thus more percolation pathways are created in the film for electron transport. This could result from the high CdSe QD loading (85 wt%) in the active layer.

We also calculated the series resistance (R_s) and shunt resistance (R_{sh}) to quantitatively understand the effect of different HTLs on the device performance. The J-V curves of the fabricated devices were measured in the dark and fitted to calculate R_s and R_{sh}. Because the difference in electron mobility (1.1×10^{-3} $cm^2(V•s)^{-1}$) and hole mobility (1.8×10^{-6} $cm^2(V•s)^{-1}$) exceeds two orders of magnitude, photocurrent reaches the fundamental space-charge limit[48]. An improved Shockley model using the space-charge approach (Eqs. S1-S3) was used to fit the dark J-V curves following the same numerical methods by W. U. Hyunh *et. al.*[49]. Typical semilog scale dark J-V plots of these solar cells are displayed in Fig. 4. The dark current at forward bias can be divided into three regions based on the voltage at the inflection points of the dark J-V curves (Fig. 4)[50]. The J-V characteristics at regions Ⅰ and Ⅲ are primarily determined by R_{sh} and R_s, respectively, and that at region Ⅱ is governed by diode parameters of the saturation current (J_0) and the ideality factor (n) that are in the improved Shockley model using the space-charge approach[49]. The fitting parameters (n and J_0) are summarized in Table S3.

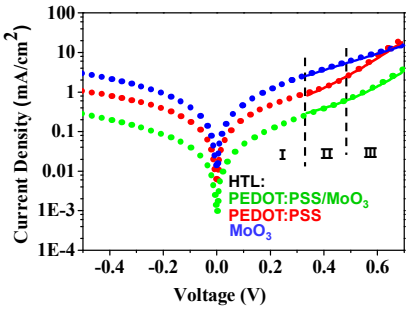

Fig. 4 Typical semilog scale J-V plots of inverted CdSe QDs:P3HT solar cells in the dark. The solid lines are fit to the regions of high forward bias using Eqs. S1-S3. Devices were fabricated with a structure of ITO/ZnO/85 wt% CdSe QDs:P3HT/HTL/Ag. A MoO_3 only, a PEDOT:PSS only, or a PEDOT:PSS/MoO_3 were used as the HTLs. The thickness of PEDOT:PSS and MoO_3 are 40 and 10 nm, respectively.

The calculated R_{sh} and R_s of the corresponding devices are listed in Table 1. Devices with MoO_3 as the HTL present the smallest R_{sh} among three types of HTLs. A small R_{sh} is often the result of pinholes present in the active layer or connected pathways between two electrodes[51] or the imperfect coverage of an HTL. Because all the devices were fabricated using the same active layer under the same conditions, the difference in R_{sh} should be predominately caused by the different HTLs. Imperfect coverage of MoO_3 could cause the small R_{sh}, which induces the current leaking through the circuit, and thus resulting in high dark current as shown in Fig. 4. In addition, devices with small R_{sh} exhibit the characteristics of a small rectification and a steep slope under reverse bias in the illuminated J-V curves (Fig. 1C). Thus, poor performance was observed in the devices with MoO_3 as the HTL. Using PEDOT:PSS as the HTL, the R_{sh} of the devices was increased by about one order of magnitude. Comparing to the devices with MoO_3 as the HTL, the devices using PEDOT:PSS as the HTL show lower dark current (Fig. 4). The lower dark current leads to the devices with higher V_{OC} by using MoO_3 as the HTL (Table 1) according to the relationship that V_{OC} is proportional to logarithmic ratio of photocurrent to dark current (Eq. S6)[52]. Moreover, the illuminated J-V becomes more flat under reverse bias and the rectification is increased (Fig. 1C). All these indicate the PEDOT:PSS layer could provide better coverage to the active layer and improve the leakage and recombination. Further improvement of R_{sh} was realized by evaporating a 10 nm layer of MoO_3 on the devices pre-coated with a 40 nm layer of PEDOT:PSS (Table 1). Devices with the dual HTL show a higher R_s (3.45 Ω) than those with PEDOT:PSS (2.05 Ω) as the HTL. The R_s includes the bulk and the contact resistance[53]. The slight increase in the R_s of devices with a dual HTL is due to an increase in the contact resistance by the insertion of a MoO_3 layer between PEDOT:PSS and Ag because all the other parts of the devices are the same. As mentioned before, the introduction of a MoO_3 layer prevents the transfer of electrons from the active layer to the anode and reduces the chance of charge recombination. Devices with the dual HTL show a lower dark current (Fig. 4) and larger V_{OC} (Table 1) than those with PEDOT:PSS as the HTL. Thus, a flat illuminated J-V curve under reverse bias and a large rectification are observed (Fig. 1C). By adopting a dual HTL, both the R_s and R_{sh} are increased. An improvement in the R_{sh} contributes to the enhancement in performance of the fabricated devices with a dual HTL since a dual HTL can best prevent leakage current and recombination in the devices. As a result, the devices with a dual HTL exhibit the best performance among the devices using the same weight ratio of CdSe QDs but different HTLs.

Photon induced charge carrier generation strongly depends on the intensity of the incidence light. Device parameters such as J_{SC}, V_{OC}, FF, and PCE were measured with a light intensity from 42 to 100 mW/cm^2 using the device with 85 wt% CdSe QDs in the BHJ layer and PEDOT:PSS/ MoO_3 as the HTL. The dependence of V_{OC} and FF on light intensity is shown in Fig. 5A and the relationship of J_{SC} and PCE with light intensity is displayed in Fig. 5B. V_{OC} increases linearly with the increase of the logarithmic light intensity while FF decreases slightly. When the V_{OC} equals the applied voltage, the internal electrical field within the devices is reduced to zero. The field

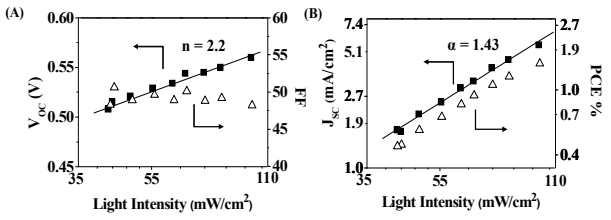

Fig. 5 (A) V_{OC} and FF as a function of logarithmic scaled light intensity. A fit of V_{OC} and logarithmic light intensity to the simple Shockley equation is shown. Ideality factor (n) is determined to be 2.2. (B) J_{SC} and PCE as a function of light intensity in a double logarithmic scale. A fit of J_{SC} and light intensity (I) to the relationship of $J_{SC} \propto I^{\alpha}$ with α = 1.43 is shown. Devices were fabricated with a structure of ITO/ZnO/85 wt% CdSe QDs:P3HT/ PEDOT:PSS/MoO_3/Ag. The thickness of PEDOT:PSS and MoO_3 are 40 and 10 nm, respectively.

dependence of the photocurrent becomes insignificant. A simple Shockley model was used to fit the linear relationship between V_{OC} and logarithmic power (Eq. S6). The ideality factor (n) was determined to be 2.2, which is greater than 2.0. The value of n = 2.62 (Table S3) was obtained using the Shockley fits in the dark, displayed in Fig. 4. An ideality factor equal to 2.0 means the recombination of charge carriers is fully trap-assisted[54, 55]. A higher ideality factor observed, which is normal in CdSe:P3HT hybrid solar cells[51], could be explained by the surface states of CdSe QDs at the p-n junction between P3HT and CdSe[56]. In conventional CdSe:P3HT hybrid solar cells, a decrease in FF from about 45 to 38 V at high intensity from ~40 to 110 mW/cm^2 was observed[49], which is a detrimental for solar cells working under high intensity such as with a solar concentrator. Only a slight decrease in FF from about 50 to 48 with the increase of the light intensity in the same range was observed in the inverted solar cells with a dual HTL (Fig. 5A). This indicates the resistive losses of the CdSe QDs:P3HT hybrid system at high illumination power are effectively prevented by adopting the structure of the inverted configuration and the dual HTL. As can be seen in Fig. 5B, J_{SC} and PCE increase linearly with increasing light intensity in a double logarithmic scale. J_{SC} is linear with illuminated light intensity, indicating there is no substantial space charge buildup by increasing the light intensity. Furthermore, a linear fit of the J_{SC} plot yields a scaling exponent α = 1.43, according to the power-law relationship of $J_{SC} \propto P_{light}^{\alpha}$, where P_{light} is the light power (or intensity). The larger than unit value could be due to the small range of light intensity. Nonetheless, this means the charge carrier losses are dominated by monomolecular recombination via defects in the active layer[57, 58]. Bimolecular recombination of electrons and holes, which reflected by α = 0.5 in the light intensity dependence of photocurrent, was not observed even at high light intensities in the inverted hybrid CdSe-polymer solar cells adopting PEDOT:PSS/MoO_3 as dual HTLs. An increase of V_{OC}, J_{SC} and slight decrease of FF result in the increase of PCE under increased light intensity.

PTB7-F20 is a fluorinated thieno[3, 4-b]thiophene copolymer[59]. The thienothiophene unit with and without F was mixed with a ratio of 2:8 in PTB7-F20. The conduction and valence band edges (E_{CB} and E_{VB}) of PTB7-F20 are -3.26 and -5.07 eV, respectively. PTB7 forms small domains in a BHJ solar cell (Fig. 6A), which facilitate the separation of electron and hole. In contrast, P3HT crystalizes in large highly crystalline polymer domains (Fig. 6B). Carriers are more likely to be trapped and recombine if no adjacent crystalline is available for them to hop to. PTB7-F20 thin films possess a hole mobility of 9.0 × 10^{-4} cm^2(V•s)$^{-1}$ [59], which is much larger than that of P3HT (1.8 × 10^{-6} cm^2(V•s)$^{-1}$). A combination of CdSe QDs and CdSe NRs as the acceptor provides an efficient network for electron transport[5, 60]. By adopting PTB7-F20 as the donor and CdSe QDs and CdSe NRs as the acceptor, the charge recombination is expected to be suppressed due to the efficient transport of both the electrons and holes. CdSe NRs with the aspect ratio of 1:10.5 (Fig. 7A) were synthesized by reacting at 250°C for 30 min. The UV-Vis and PL spectra of the synthesized CdSe NRs with the reaction time from 1 to 30 min were shown in Fig. S4A and B in the Support Information, respectively. The first excitonic absorption peak shifts from 524 to 613 nm by reacting at 250°C from 1 to 30 min. The corresponding PL emission shifts to longer wavelength by prolonged reaction time. Devices were fabricated in an inverted structure of ITO/ZnO/CdSe QDs or CdSe QDs + NRs:PTB7-F20/PEDOT:PSS/MoO_3/Ag. Typical J-V characteristics of devices were recorded and displayed in Fig. 7B. For the device containing 85 wt% CdSe QDs with the dual HTL, a J_{SC} of 3.9±0.2 mA/cm^2, a V_{OC} of 0.68±0.01 V and a FF of 51.5±2.2% were observed, which led to a PCE of 1.38±0.21%. Devices fabricated using PTB7-F20 as the donor consistently show higher V_{OC} and FF (Table 2) than those fabricated using P3HT (Table 1). This may be ascribed to the enhanced intramolecular charge separation and reduced charge recombination enabled by PTB7-F20. The device performance is improved by using a combination of CdSe QDs and CdSe NRs. The V_{OC} and FF were lightly increased to 0.70±0.02 V and 52.9±1.1%, respectively. A dramatic increase in the J_{SC} from 3.9±0.2 to 5.5±0.3 mA/cm^2 led to an overall PCE of 2.03±0.33%. Higher J_{SC}'s and better PCEs in devices based on a combination of QDs + NRs were also observed by other groups[5, 60]. The increase in the observed J_{SC} could be explained by the facile electron transport enabled by the percolation pathway network formed by interconnecting the parallel-aligned NRs with QDs.

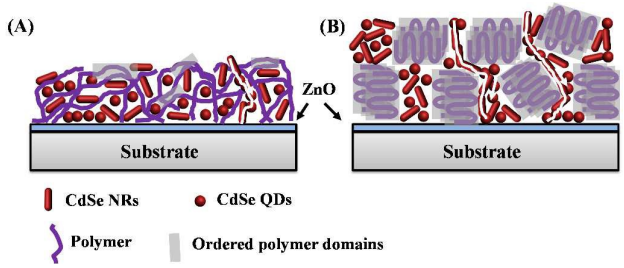

Fig. 6 Schematic illustration of the morphology dependence of (A) CdSe QDs + CdSe NRs:PTB7-F20 film and (B) CdSe QDs + CdSe NRs:P3HT film on the substrate coated with ZnO layer. The percolation pathways were marked as white lines in the illustrations. Electrons were collected by the cathode through a ZnO layer.

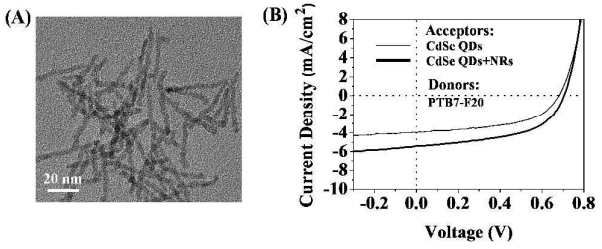

Fig. 7 (A) The TEM image of CdSe NRs synthesized with the aspect ratio of 1:10.5. (B) Typical J-V characteristics of the inverted CdSe:PTB7-F20 solar cells under AM 1.5G 1 sun illumination. Devices were fabricated with a structure of ITO/ZnO/85 wt% CdSe:PTB7-F20/PEDOT:PSS/MoO_3/Ag. CdSe QDs or a CdSe QDs + CdSe NRs (weight ratio = 2:1) were used as the acceptors. The thickness of PEDOT:PSS and MoO_3 are 40 and 10 nm, respectively.

Table 2 Summary of the performance parameters of inverted CdSe:PTB7-F20 solar cells under AM 1.5G 1 sun illumination. Devices were fabricated with a structure of ITO/ZnO/85 wt% CdSe:PTB7-F20/ PEDOT:PSS/MoO_3/Ag. CdSe QDs or a CdSe QDs + CdSe NRs (weight ratio = 2:1) were used as the acceptors. The thickness of PEDOT:PSS and MoO_3 are 40 and 10 nm, respectively.

Acceptor	V_{OC} (V)	J_{SC} (mA/cm^2)	FF (%)	PCE (%)	PCE_{max} (%)
CdSe QDs	0.68±0.01	3.9±0.2	51.5±2.2	1.38±0.21	1.59
CdSe QDs+NRs	0.70±0.02	5.5±0.3	52.9±1.1	2.03±0.33	2.35

Conclusions

In summary, inverted hybrid CdSe-polymer solar cells with a dual HTL of PEDOT:PSS/MoO_3 showed better performance than those with a single HTL of PEDOT:PSS or MoO_3. More complete surface coverage provided by the PEDOT:PSS layer plus the enhanced electron blocking provided by the MoO_3 layer account for the improved device performance enabled by such a dual HTL. Study on the relationship of V_{OC}, J_{SC}, FF, and PCE as a function of light intensity indicated that the resistive losses of the CdSe QDs:P3HT hybrid system at high illumination power were effectively prevented by adopting the inverted structure and using the dual HTL. Further study showed that the dual HTL is applicable to hybrid CdSe:PTB7-F20 solar cells. An efficiency as high as 2.35% was reached by inverted hybrid CdSe:PTB7-F20 solar cells with a structure of ITO/ZnO/CdSe QDs + NRs:PTB7-F20/ PEDOT:PSS/MoO_3/Ag. The concept of a dual HTL could be applied to other organic and hybrid solar cell systems in order to achieve high device performance.

Acknowledgements

The authors thank the financial support from the American Chemical Society Petroleum Research Funds (ACS PRF) and the National Science Foundation (NSF, CBET 1346859). TEM images were taken at the Nanotech User Facility, the UW site of the National Nanotechnology Infrastructure Network (NNIN) supported by the NSF. UV–Vis–NIR absorption and PL measurements were carried out in the UW Department of Chemistry's Spectroscopic and Analytical Instrumentation facility. Device fabrication and performance measurements were carried out in the UW Photonics Research Facility. EQE measurements were conducted in the lab of Professor Alex Jen.

Notes and references

1 L.-S. Li, J. Hu, W. Yang and A. P. Alivisatos, *Nano Lett.*, 2001, **1**, 349.
2 W. U. Huynh, J. J. Dittmer and A. P. Alivisatos, *Science*, 2002, **295**, 2425.
3 G. Dennler, M. C. Scharber and C. J. Brabec, *Adv. Mater.*, 2009, **21**, 1323.
4 B. J. Richardson, L. Zhu and Q. Yu, *Sol. Energy Mater. Sol. Cells*, 2013, **116**, 252.
5 K. F. Jeltsch, M. Schädel, J. B. Bonekamp, P. Niyamakom, F. Rauscher, H. W. Lademann, I. Dumsch, S. Allard, U. Scherf and K. Meerholz, *Adv. Funct. Mater.*, 2012, **22**, 397.
6 S. Dayal, N. Kopidakis, D. C. Olson, D. S. Ginley and G. Rumbles, *Nano Lett.*, 2009, **10**, 239.
7 L. Han, D. Qin, X. Jiang, Y. Liu, L. Wang, J. Chen and Y. Cao, *Nanotechnology*, 2006, **17**, 4736.
8 J. Liu, T. Tanaka, K. Sivula, A. P. Alivisatos and J. M. Fréchet, *J. Am. Chem. Soc.*, 2004, **126**, 6550.
9 M. Wright and A. Uddin, *Sol. Energy Mater. Sol. Cells*, 2012, **107**, 87.
10 S. Dowland, T. Lutz, A. Ward, S. P. King, A. Sudlow, M. S. Hill, K. C. Molloy and S. A. Haque, *Adv. Mater.*, 2011, **23**, 2739.
11 S. Ren, L.-Y. Chang, S.-K. Lim, J. Zhao, M. Smith, N. Zhao, V. Bulović, M. Bawendi and S. Gradečak, *Nano Lett.*, 2011, **11**, 3998.
12 A. A. Watt, D. Blake, J. H. Warner, E. A. Thomsen, E. L. Tavenner, H. Rubinsztein-Dunlop and P. Meredith, *J. Phys. D: Appl. Phys.*, 2005, **38**, 2006.
13 J. Halls, C. Walsh, N. Greenham, E. Marseglia, R. Friend, S. Moratti and A. Holmes, *Nature*, 1995, **376**, 498.
14 M. P. de Jong, L. J. van IJzendoorn and M. J. A. de Voigt, *Appl. Phys. Lett.*, 2000, **77**, 2255.
15 S. K. Hau, H.-L. Yip, N. S. Baek, J. Zou, K. O'Malley and A. K.-Y. Jen, *Appl. Phys. Lett.*, 2008, **92**, 253301.
16 R. Lazzaroni, M. Lögdlund, A. Calderone, J. L. Brédas, P. Dannetun, C. Fauquet, C. Fredriksson, S. Stafström and W. R. Salaneck, *Synt. Met.*, 1995, **71**, 2159.
17 P. Dannetun, M. Boman, S. Stafström, W. R. Salaneck, R. Lazzaroni, C. Fredriksson, J. L. Brédas, R. Zamboni and C. Taliani, *J. Chem. Phys.*, 1993, **99**, 664.
18 Z. Zhao, Q. Wu, F. Xia, X. Chen, Y. Liu, W. Zhang, J. Zhu, S. Dai and S. Yang, *ACS Appl. Mater. Interfaces*, 2015, **7**, 1439.
19 Y. Sun, S.-C. Chien, H.-L. Yip, Y. Zhang, K.-S. Chen, D. F. Zeigler, F.-C. Chen, B. Lin and A. K.-Y. Jen, *Chem. Mater.*, 2011, **23**, 5006.
20 L. S. Pingree, B. A. MacLeod and D. S. Ginger, *J. Phys. Chem. C*, 2008, **112**, 7922.
21 S. K. Hau, H.-L. Yip, J. Zou and A. K.-Y. Jen, *Org. Electron.*, 2009, **10**, 1401.
22 K. Norrman, M. V. Madsen, S. A. Gevorgyan and F. C. Krebs, *J. Am. Chem. Soc.*, 2010, **132**, 16883.
23 M. D. Irwin, D. B. Buchholz, A. W. Hains, R. P. Chang and T. J. Marks, *Proc. Natl. Acad. Sci.*, 2008, **105**, 2783.
24 J. R. Manders, S.-W. Tsang, M. J. Hartel, T.-H. Lai, S. Chen, C. M. Amb, J. R. Reynolds and F. So, *Adv. Funct. Mater.*, 2013, **23**, 2993.

25 J. Meyer, R. Khalandovsky, P. Görrn and A. Kahn, *Adv. Mater.*, 2011, **23**, 70.
26 K. Zilberberg, S. Trost, H. Schmidt and T. Riedl, *Adv. Energy Mater.*, 2011, **1**, 377.
27 C. Tao, S. Ruan, G. Xie, X. Kong, L. Shen, F. Meng, C. Liu, X. Zhang, W. Dong and W. Chen, *Appl. Phys. Lett.*, 2009, **94**, 043311.
28 T. Stubhan, T. Ameri, M. Salinas, J. Krantz, F. Machui, M. Halik and C. J. Brabec, *Appl. Phys. Lett.*, 2011, **98**, 253308.
29 S. Chen, K. R. Choudhury, J. Subbiah, C. M. Amb, J. R. Reynolds and F. So, *Adv. Energy Mater.*, 2011, **1**, 963.
30 S. Chen, C. E. Small, C. M. Amb, J. Subbiah, T.-h. Lai, S.-W. Tsang, J. R. Manders, J. R. Reynolds and F. So, *Adv. Energy Mater.*, 2012, **2**, 1333.
31 M. Schierhorn, S. W. Boettcher, J. H. Peet, E. Matioli, G. C. Bazan, G. D. Stucky and M. Moskovits, *ACS Nano*, 2010, **4**, 6132.
32 C. Liu, J. Li, X. Zhang, Y. He, Z. Li, H. Li, W. Guo, L. Shen and S. Ruan, *Phys. Chem. Chem. Phys.*, 2015, **17**, 7960.
33 Y. Wang, Q. Luo, N. Wu, Q. Wang, H. Zhu, L. Chen, Y.-Q. Li, L. Luo and C.-Q. Ma, *ACS Appl. Mater. Interfaces*, 2015, **7**, 7170.
34 S. Roy, A. Aguirre, D. A. Higgins and V. Chikan, *J. Phys. Chem. C*, 2012, **116**, 3153.
35 R. Zhou, Y. Zheng, L. Qian, Y. Yang, P. H. Holloway and J. Xue, *Nanoscale*, 2012, **4**, 3507.
36 J. Yang, A. Tang, R. Zhou and J. Xue, *Sol. Energy Mater. Sol. Cells*, 2011, **95**, 476.
37 L. Qian, J. Yang, R. Zhou, A. Tang, Y. Zheng, T.-K. Tseng, D. Bera, J. Xue and P. H. Holloway, *J. Mater. Chem.*, 2011, **21**, 3814.
38 W. W. Yu, L. Qu, W. Guo and X. Peng, *Chem. Mater.*, 2003, **15**, 2854.
39 M. J. Greaney, S. Das, D. H. Webber, S. E. Bradforth and R. L. Brutchey, *ACS Nano*, 2012, **6**, 4222.
40 Y. Zhou, F. S. Riehle, Y. Yuan, H.-F. Schleiermacher, M. Niggemann, G. A. Urban and M. Krüger, *Appl. Phys. Lett.*, 2010, **96**, 013304.
41 N. C. Greenham, X. Peng and A. P. Alivisatos, *Phys. Rev. B*, 1996, **54**, 17628.
42 L. Zhu, B. J. Richardson and Q. Yu, *Nanoscale*, 2014, **6**, 1029.
43 L. Brus, *J. Phys. Chem.*, 1986, **90**, 2555.
44 P. Murgatroyd, *J. Phys. D: Appl. Phys.*, 1970, **3**, 151.
45 K. Kumari, S. Chand, V. Vankar and V. Kumar, *Appl. Phys. Lett.*, 2009, **94**, 213503.
46 W. Fu, Y. Shi, W. Qiu, L. Wang, Y. Nan, M. Shi, H. Li and H. Chen, *Phys. Chem. Chem. Phys.*, 2012, **14**, 12094.
47 E. Talgorn, R. D. Abellon, P. J. Kooyman, J. Piris, T. J. Savenije, A. Goossens, A. J. Houtepen and L. D. Siebbeles, *ACS Nano*, 2010, **4**, 1723.
48 V. Mihailetchi, J. Wildeman and P. Blom, *Phys. Rev. Lett.*, 2005, **94**, 126602.
49 W. U. Huynh, J. J. Dittmer, N. Teclemariam, D. J. Milliron, A. P. Alivisatos and K. W. Barnham, *Phys. Rev. B*, 2003, **67**, 115326.
50 J. D. Servaites, M. A. Ratner and T. J. Marks, *Energy Environ. Sci.*, 2011, **4**, 4410.
51 J. Y. Lek, Y. M. Lam, J. Niziol and M. Marzec, *Nanotechnology*, 2012, **23**, 315401.
52 N. Li, B. E. Lassiter, R. R. Lunt, G. Wei and S. R. Forrest, *Appl. Phys. Lett.*, 2009, **94**, 023307.
53 D. Chirvase, J. Parisi, J. C. Hummelen and V. Dyakonov, *Nanotechnology*, 2004, **15**, 1317.
54 G. A. H. Wetzelaer, M. Kuik, H. T. Nicolai and P. W. M. Blom, *Phys. Rev. B*, 2011, **83**, 165204.
55 M. Kuik, H. T. Nicolai, M. Lenes, G.-J. A. H. Wetzelaer, M. Lu and P. W. M. Blom, *Appl. Phys. Lett.*, 2011, **98**, 093301.
56 A. Jain and A. Kapoor, *Sol. Energy Mater. Sol. Cells*, 2005, **85**, 391.
57 I. Riedel, J. Parisi, V. Dyakonov, L. Lutsen, D. Vanderzande and J. C. Hummelen, *Adv. Funct. Mater.*, 2004, **14**, 38.
58 I. Riedel and V. Dyakonov, *Phys. Status Solidi A*, 2004, **201**, 1332.
59 H. Wang, X. Yu, C. Yi, H. Ren, C. Liu, Y. Yang, S. Xiao, J. Zheng, A. Karim and S. Z. Cheng, *J. Phys. Chem. C*, 2013, **117**, 4358.
60 Y. Zhou, M. Eck, C. Men, F. Rauscher, P. Niyamakom, S. Yilmaz, I. Dumsch, S. Allard, U. Scherf and M. Krüger, *Sol. Energy Mater. Sol. Cells*, 2011, **95**, 3227.